LAWRENCE
LIVERMORE
NATIONAL
LABORATORY

LLNL-JRNL-653449

Determination of the asymptotic normalization coefficients for 14C + n <> 15C, the 14C(n,(gamma))15C reaction rate, and evaluation of a new method to determine spectroscopic factors

M. McCleskey, A. M. Mukhamedzhanov, L. Trache, R. E. Tribble, A. Banu, V. Eremenko, V. Z. Goldberg, Y. W. Lui, E. McCleskey, B. T. Roeder, A. Spiridon, F. Carstoiu, V. Burjan, Z. Hons, I. J. Thompson

April 23, 2014

Physical Review C

Disclaimer

Determination of the asymptotic normalization coefficients for $^{14}C + n \leftrightarrow {}^{15}C$, the $^{14}C(n,\gamma)^{15}C$ reaction rate, and evaluation of a new method to determine spectroscopic factors

M. McCleskey,* A. M. Mukhamedzhanov,* L. Trache,† R. E. Tribble, A. Banu,‡ V. Eremenko,§ V. Z. Goldberg, Y.-W. Lui, E. McCleskey, B. T. Roeder, and A. Spiridon
Texas A&M Cyclotron Institute, College Station, Texas 77843, USA

F. Carstoiu
National Institute for Physics and Nuclear Engineering "Horia Hulubei," Bucharest-Magurele, Romania

V. Burjan and Z. Hons
Nuclear Physics Institute, Czech Academy of Sciences, CZ-250 68 Řež near Prague, Czech Republic

I. J. Thompson
Lawrence Livermore National Laboratory, Livermore, California 94550, USA

The $^{14}C + n \leftrightarrow {}^{15}C$ system has been used as a test case in the evaluation of a new method to determine spectroscopic factors that uses the asymptotic normalization coefficient (ANC). The method proved to be unsuccessful for this case. As part of this experimental program, the ANCs for the ^{15}C ground state and first excited state were determined using a heavy-ion neutron transfer reaction as well as the inverse kinematics (d,p) reaction, measured at the Texas A&M Cyclotron Institute. The values $C^2_{2s1/2} = 1.88 \pm 0.18$ fm^{-1} for the ground state and $C^2_{1d5/2} = 4.25 \pm 0.38 \times 10^{-3}$ fm^{-1} for the first excited state ($E_{exc} = 740$ keV) were obtained. The ANCs were used to evaluate the astrophysical direct neutron capture rate on ^{14}C, which was then compared with the most recent direct measurement and found to be in good agreement. A study of the ^{15}C SF via its mirror nucleus ^{15}F and a new insight into deuteron stripping theory are also presented.

PACS number(s): 21.10.Jx, 25.70.−z, 25.45.−z, 24.50.+g

I. INTRODUCTION

The $^{14}C(n,\gamma)^{15}C$ direct radiative capture reaction is thought to be important in a variety of astrophysical scenarios. Among those are inhomogeneous big-bang nucleosynthesis (IBBN) [1], depletion of carbon-nitrogen-oxygen (CNO) cycle isotopes in asymptotic giant branch (AGB) stars [2], and production of seed nuclei for possible r process in core-collapse supernovae [3]. Additionally, this reaction is useful as a benchmark for indirect methods to determine astrophysical neutron capture rates. A large disagreement between direct measurement, indirect measurements, and theory persisted for many years as the result of an error in the early direct measurement [4]. This measurement was later repeated [5].

Asymptotic normalization coefficients (ANCs) were shown to be a useful tool in determining low-energy proton direct-capture rates (see, for example, Ref. [6]) because, at low energies, proton capture is a peripheral process whose rate is governed by the asymptotic tail of the radial overlap function. Likewise, if a direct neutron capture reaction is peripheral owing to an angular momentum barrier resulting from s-wave capture being inhibited by selection rules, it, too, can be determined using the ANC. Such is the case for $^{14}C(n,\gamma)^{15}C$, which is dominated by p-wave capture [7].

Usually transfer angular distributions are analyzed within the framework of the distorted-wave Born approximation (DWBA), continuum discretized coupled channels (CDCC), or the adiabatic model. The SF determined by the normalization of the calculated differential cross section to the experimental cross section is compared with the SF predicted by the shell model. Even when error bars in the experimental cross section are low, the uncertainty of the extracted SF resulting from the normalization of the calculated cross section is often large owing to the following inaccuracies: (i) optical potential ambiguities, (ii) the inadequacy of the reaction theory, and (iii) the dependence on the single-particle potential parameters. We concentrate here on the third point considering the DWBA.

In the standard approach the parametrization of the DWBA reaction amplitude $A(d,p)F$ in terms of the SF comes as a result of the approximation of the radial overlap function

$$I_{lj} = S_{lj}\phi_{nlj}(r), \tag{1}$$

where S_{lj} is the single-particle spectroscopic factor of the configuration $n + A$ in F and ϕ_{nlj} is the neutron radial bound-state wave function calculated in the adopted mean-field potential. Because the squares of the norms of the radial overlap function and the radial bound-state wave function are, correspondingly, the spectroscopic factor and unity, the single-particle spectroscopic factor in Eq. (1) will equal the

*Corresponding authors: mmccleskey@umm.edu, akram@comp.tamu.edu
†Also at the National Institute for Physics and Nuclear Engineering, Bucharest-Magurele, Romania.
‡Present address: Department of Physics and Astronomy, James Madison University, Harrisonburg, VA 22807.
§Present address: INPP, Ohio University, Athens, OH 45701.

spectroscopic factor if the radial bound-state wave function and the radial overlap function have very similar radial behavior in both the nuclear interior, $r < R_N$, and the exterior. However, in the nuclear interior and near the nuclear surface, where both the overlap function and the bound-state wave function have most of their probability, the radial dependence of the overlap function and single-particle wave function, *a priori*, are different because the overlap function is a many-particle object, whereas the single-particle wave function is a solution of the single-particle Schrödinger equation. Thus, in general, the single-particle spectroscopic factor does not coincide with the spectroscopic factor microscopically calculated as the square of the norm of the overlap function. Nonetheless, for $r > R_N$, the radial dependencies of the radial overlap function and the radial bound-state wave function are the same, and they differ only by their overall normalizations. The asymptotic behavior of the radial overlap function and the radial bound-state wave function are given by

$$I_{lj}(r) \xrightarrow{r>R_N} C_{lj} i\kappa h_l^{(1)}(i\kappa r) \tag{2}$$

and

$$\phi_{nlj}(r) \xrightarrow{r>R_N} b_{nlj} i\kappa h_l^{(1)}(i\kappa r), \tag{3}$$

correspondingly. Here C_{lj} is the ANC for the neutron removal, b_{nlj} is the single-particle ANC, l,j are the orbital angular and total angular momentum of the neutron, respectively, n is the principal quantum number of the neutron orbital, $\kappa = \sqrt{2\mu_{nA}\eta_{nA}}$ is the bound-state wave number, η_{nA} is the neutron binding energy, and μ_{nA} is the reduced mass of n and A. Then, comparing Eqs. (1)–(3), we get

$$S = \frac{C_{lj}^2}{b_{nlj}^2}. \tag{4}$$

While the ANC is an experimentally measurable quantity, the single-particle ANC b_{nlj} is not. Hence, the single-particle SF, when defined by Eq. (4), is model dependent. Its model dependence comes through the single-particle ANC b_{nlj}, which is a function of the geometric parameters, radius r_0 and diffuseness a, of the Woods-Saxon potential conventionally used as a single-particle potential. Furthermore, note that, unlike the SF determined through the norm of the overlap function, the single-particle SF S_{lj} as defined in Eq. (4) is actually a property of the peripheral part of the neutron overlap function.

In the standard approach, which is described and used in Refs. [8,9], Eq. (4) is neglected and the single-particle SF is determined by normalization of the calculated differential cross section to the experimental cross section at the main stripping peak of the angular distribution and, hence, is a function of the adopted single-particle potential. Because the ANC determines the normalization of the external part of the reaction amplitude, which typically gives the dominant contribution to the total nucleon transfer amplitude, neglecting Eq. (4) may provide the SF at the expense of a wrong external contribution. As an example we mention the critical analysis of the SF determination for the reaction ^{48}Ca$(d,p)^{49}$Ca. In the standard analysis used in Ref. [9], the adopted geometry of the single-particle potential was $r_0 = 1.25$ fm and $a = 0.65$ fm. The determined single-particle SF was 0.62 ± 0.07. For the adopted geometry the square of the neutron single-particle ANC is 33.52 fm^{-1}, which, according to Eq. (4), leads to the square of the neutron ANC $C_{13/2}^2 = 20.8 \pm 2.3$ fm^{-1}, while the experimental value is $C_{13/2}^2 = 32.1 \pm 3.2$ fm^{-1} [10]. This instructive example clearly demonstrates the shortcoming of the standard procedure for the determination of the SF.

In this paper we test a combined method for the determination of the SF, which fixes correctly the external contribution to the reaction amplitude by taking into account Eq. (4) [11]. This procedure allows us to critically test the reliability of the determination of SFs from the nucleon transfer reactions because now its accuracy depends on how accurately the internal part of the reaction amplitude is calculated. Using the $^{15}\mathrm{C} \leftrightarrow {}^{14}\mathrm{C} + n$ system as a test case for this new method has the benefit of allowing the evaluation of the astrophysical $^{14}\mathrm{C}(n,\gamma)^{15}\mathrm{C}$ reaction rate using the ANC.

To accomplish this, three reactions were measured. For the determination of the ANC, the heavy-ion (HI) neutron transfer reaction $^{13}\mathrm{C}(^{14}\mathrm{C},^{15}\mathrm{C})^{12}\mathrm{C}$ at 12 MeV/nucleon and the inverse kinematics reaction $d(^{14}\mathrm{C},p)^{15}\mathrm{C}$ at 11.7 MeV/nucleon were used. To evaluate the new method, the less peripheral reaction $^{14}\mathrm{C}(d,p)^{15}\mathrm{C}$ with $E_d = 60$ MeV was also measured.

II. DETERMINING THE ANC FOR $^{15}\mathrm{C} \leftrightarrow {}^{14}\mathrm{C} + n$

A. $^{13}\mathrm{C}(^{14}\mathrm{C},^{15}\mathrm{C})^{12}\mathrm{C}$

This measurement was performed using a 12 MeV/nucleon ^{14}C beam from the K500 superconducting cyclotron at TAMU-CI. This energy was selected to ensure that the reaction was peripheral and because of significant past experience with nucleon transfer reactions around this energy [12]. After the cyclotron, the beam analysis system (BAS) [13] was used to improve the momentum and position resolution of the beam, which was then transported to the multipole-dipole-multipole (MDM) spectrometer [14]. The beam was focused on a 104 ± 4 μg/cm^2 ^{13}C target. The Oxford detector [15], an ionization chamber detector, was placed in the focal plane of the spectrometer and filled with isobutane gas at a pressure of 50 torr. The energy loss of the reaction products in the gas plotted against their energy when stopped in a plastic scintillator after the detector was used for particle identification and is shown in Fig. 1. Because of the similar magnetic rigidities of the ^{14}C elastic scattering and the ^{15}C reaction products, both were accepted into the detector and were measured at the same time. Four position-sensitive avalanche counters inside the detector were used to measure the angle and reconstruct the position in the focal plane of the spectrometer. This information was also used in a raytrace reconstruction of the angle of the reaction products after the target, which was used to extract the angular distribution.

The ANC, C_{lj}, is defined as the ratio of the overlap function, I_{lj}, to a Whittaker function for a Sommerfeld parameter η, orbital angular momentum l, and wave number $\kappa = \sqrt{2\mu_{Ax}\epsilon_B}$ of the particle(x)-core(A) relative motion that is evaluated at a radius, r, larger than the nuclear radius R_N,

$$I_{lj}(r) \overset{r>R_N}{\to} C_{lj} \frac{W_{-\eta,(l+1/2)}(2\kappa r)}{r}. \tag{5}$$

In the case of a neutron-core system, it is given by Eq. (2).

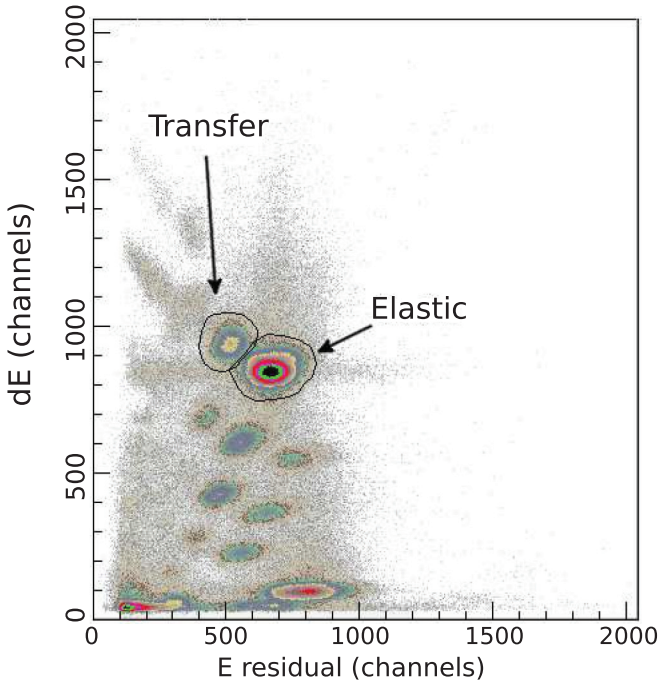

FIG. 1. (Color online) ΔE-E particle identification for the HI measurement.

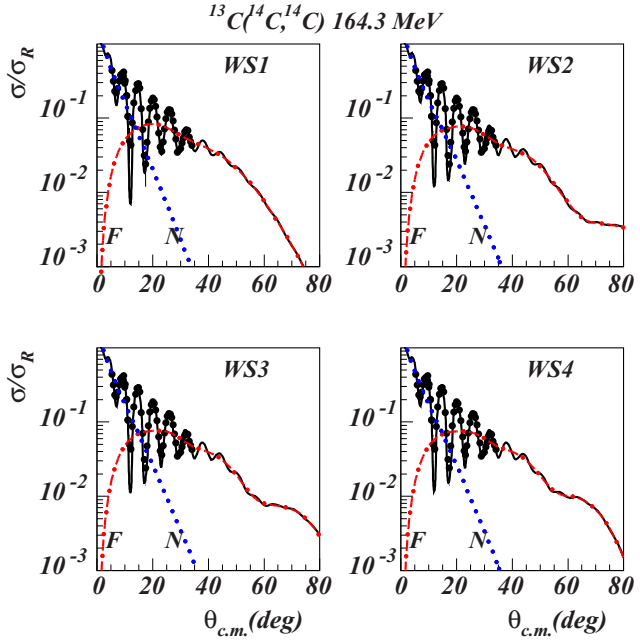

FIG. 2. (Color online) Experimental data points for the elastic scattering of 12 MeV/nucleon ^{14}C on ^{13}C are shown as black dots. The calculated distributions resulting from the grid search are shown decomposed into near (dotted blue line) and far (dot-dashed red line) distributions and their coherent sum (solid black line).

This leads to a parametrization of the cross section of a peripheral reaction $A(a,b)B$, where a nucleon x is transferred from a to A, in terms of the ANCs [16],

$$\frac{d\sigma}{d\Omega} = \sum_{j_B l_B} \left(C^B_{Axl_B j_B}\right)^2 \left(C^a_{bxl_a j_a}\right)^2 \frac{\sigma^{\rm DW}_{l_B j_B l_a j_a}}{b^2_{Axl_B j_B} b^2_{bxl_a j_a}}. \quad (6)$$

Here $\sigma_{\rm DW}$ is the calculated DWBA cross section, C is the ANC, and l and j are orbital and total angular momentum, respectively. To find the ANC for $^{15}{\rm C} \leftrightarrow {}^{14}{\rm C} + n$ from ^{13}C(^{14}C,^{15}C)^{12}C requires the ANC for $^{13}{\rm C} \leftrightarrow {}^{12}{\rm C} + n$, which is $C^2 = 2.31 \pm 0.08$ fm^{-1} [17].

The dominant source of uncertainty in the DWBA calculation of the angular distribution of the transfer and thus in the ANC is the choice of the optical model potential (OMP), which generates the distorted wave in the entrance and exit channels. Two approaches to find an OMP from the measured elastic scattering data were used here. The first, a phenomenological grid search in real potential depth used an OMP of the form

$$U_{\rm OMP} = V + iW, \quad (7)$$

where V and W are of the Wood-Saxon form

$$V_{\rm WS} = -\frac{V_0}{1 + \exp\left(\frac{r - R_0}{a_0}\right)}. \quad (8)$$

In this grid search a fit was made of the five remaining parameters at each point. The results were families of continuously ambiguous potentials with similar quality fits for a large variety of real potential depths. As a result, five depths were arbitrarily chosen for further fitting, resulting in five final OMPs for this approach, which are shown in Table I. The elastic angular distributions calculated from these OMPs are plotted against the experimental data in Fig. 2. For all angular distributions shown for this HI measurement (both elastic scattering and neutron transfer), the experimental uncertainty is smaller than the data points and thus error bars are not plotted.

The second approach was a semimicroscopic double-folding (DF) calculation using the Jeukenne, Lejeune, and Mahaux (JLM) effective interaction as described in Ref. [12]. This approach has the advantage of having fewer parameters

TABLE I. Optical model potential parameters for 12 MeV/nucleon ^{14}C elastic scattering on ^{13}C.

	V (MeV)	W (MeV)	r_v (fm)	r_w (fm)	a_v (fm)	a_w (fm)	χ^2	J_v (MeV fm^3)	R_v (fm)	J_w (MeV fm^3)	R_w (fm)
WS1	77.1	13.32	0.987	1.209	0.703	0.723	3.09	225	4.480	68	5.206
WS2	118.7	14.15	0.927	1.191	0.690	0.739	3.4	292	4.275	69	5.182
WS3	162.4	15.03	0.891	1.169	0.674	0.767	3.59	357	4.132	71	5.169
WS4	203.1	16.04	0.894	1.133	0.627	0.825	3.6	438	4.038	71	5.183
WS5	248.8	16.66	0.885	1.115	0.606	0.848	3.65	516	3.965	72	5.180
DF	141.43	45.72	0.735	0.812	0.920	1.020	3.4				

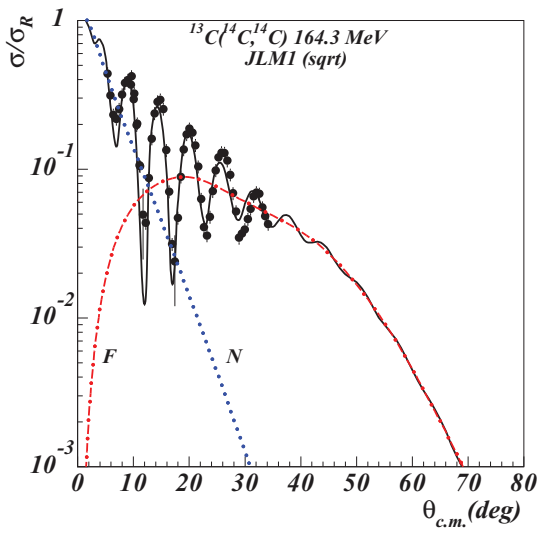

FIG. 3. (Color online) Result of the DF calculation for elastic scattering of 12 MeV/nucleon ^{14}C on ^{13}C shown decomposed into near (dotted blue line) and far (dot-dashed red line) distributions and the coherent sum (solid black line).

to fit (either two or four, depending on whether the ranges are kept fixed at the best values given in Ref. [12], as was done here). After fitting to the elastic scattering, the potential is fit in the surface region to a WS form, which is then used in the DWBA calculation of the transfer. The DWBA calculation was performed using the code PTOLEMY [18]. The fit of the elastic angular distribution from this approach and the measured distribution are shown in Fig. 3 and the results of the DWBA calculations for all of the potentials are plotted with the transfer in Fig. 4 (ground state) and Fig. 5 (first excited state). We restricted the analysis to the $J^\pi = 1/2^+$ ground state and $J^\pi = 5/2^+$ first and only particle bound excited state ($E_{\rm exc} = 740$ keV [19]) of ^{15}C. In calculations the orbitals $2s_{1/2}$ and $1d_{5/2}$, respectively, were considered. The resulting OMPs of both approaches and the extracted ANCs are summarized in Tables I and II. The same OMP was used in both the entrance and exit channel for each case.

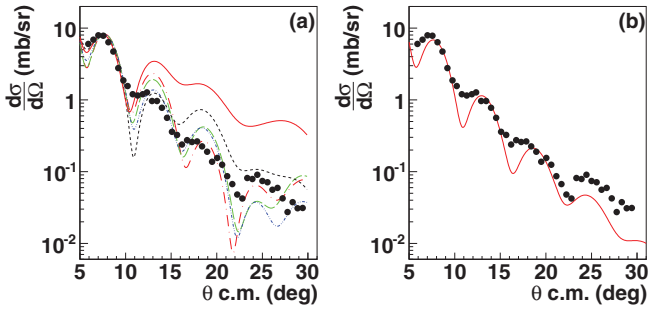

FIG. 4. (Color online) The calculated distributions for ^{13}C(^{14}C,^{15}C)^{12}C ($E_{^{14}\rm C} = 12$ MeV/nucleon) neutron transfer to the ground state have been normalized to the experimental data from 5° to 11°. Calculations using the WS potentials from the grid search are shown in (a); those using DF are shown in (b).

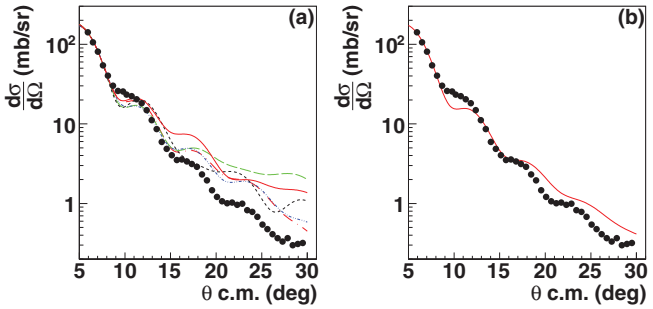

FIG. 5. (Color online) The calculated distributions for ^{13}C(^{14}C,^{15}C)^{12}C ($E_{^{14}\rm C} = 12$ MeV/nucleon) neutron transfer to the first excited state normalized to the experimental data. Calculations using the WS potentials from the grid search are shown in (a); those using DF are shown in (b).

Sources of uncertainty in this measurement were target thickness (4%), normalization to the number of incident particles (3%), data extraction and disentanglement from the first excited state of ^{15}C (5%), statistical uncertainty (6% for the ground state and 1% for the first excited state), and a systematic uncertainty from the calculation evaluated based on the variation of the results owing to the choice of optical potential (10%). These independent sources of uncertainty added in quadrature give an overall uncertainty in the ANC^2 of 14% for the ground state and 13% for the first excited state.

B. $d(^{14}\mathrm{C},p)^{15}\mathrm{C}$

The measurement of the angular distribution for the inverse kinematics (d,p) reaction on ^{14}C was performed as the commissioning run for the Texas A&M-Edinburgh-Catania-Silicon-Array (TECSA). A ^{14}C beam of 11.7 MeV/nucleon impinged on a 251 ± 5 μg/cm^2 CD_2 target. At this beam energy this reaction is peripheral. The protons were detected in the backwards (lab) direction by the high-efficiency array of silicon detectors from 102° to 165° laboratory angle (4.5° to 32.2° c.m.). As in the HI neutron transfer reaction described in the previous section, both transfer to the ground state and first excited state were measured. More details of the apparatus and this experiment are given in Ref. [20]. The angular distributions were calculated using the code FRESCO [21]. The adiabatic distorted wave approximation (ADWA) [22] was used for the entrance channel utilizing CH89 [23] and

TABLE II. Phenomenological SFs and ANCs obtained with DWBA calculation using the OMPs.

	$SF_{2s1/2}$	$C^2_{2s1/2}$ (fm^{-1})	$SF_{1d5/2}$	$C^2_{1d5/2}$ (fm^{-1})
WS1-WS1	1.22	2.30	1.13	4.45×10^{-3}
WS2-WS2	1.16	2.18	1.02	4.03×10^{-3}
WS3-WS3	1.04	1.95	1.13	4.46×10^{-3}
WS4-WS4	0.98	1.83	1.20	4.74×10^{-3}
WS5-WS5	1.14	2.14	1.25	4.94×10^{-3}
DF	1.15	2.16	1.09	4.28×10^{-3}
Average	1.12	f2.09	1.14	4.48×10^{-3}

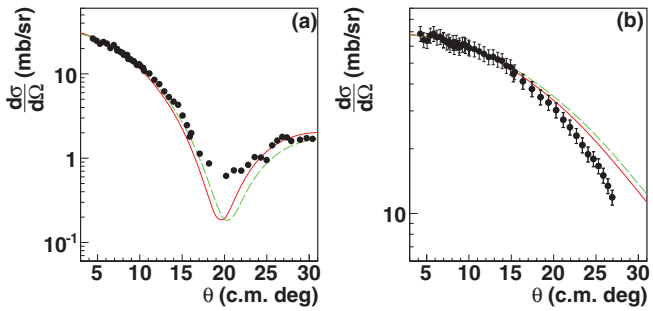

FIG. 6. (Color online) Shown in (a) is the angular distribution for $d(^{14}\mathrm{C},p)^{15}\mathrm{C}$ ($E_{^{14}\mathrm{C}} = 11.7$ MeV/nucleon) transfer to the $2s1/2$ ground state. Black dots mark the experimental data points and the solid red line is the ADWA calculation using CH89 potential, while the dashed green line is a similar calculation with KD03 potentials. Uncertainty in the experimental data is smaller than the data points and is not plotted. Shown in (b) is the same for the 740-keV $1d5/2$ first excited state; however, experimental uncertainty is larger than the data points and is shown.

Koning-Delaroche (KD03) [24] single nucleon potentials for the proton and neutron evaluated at half the deuteron energy. The finite range correction described in Ref. [25] was applied to the potential for the entrance channel. The experimental and renormalized calculations are shown in Fig. 6, and the resulting ANCs are given in Table III.

The overall experimental uncertainty for the measured differential cross section was 8%, which consisted of 2% owing to target thickness, 2% to 6% from the incident beam normalization, 4% for the analysis, and <2% for statistics. This combined with a 10% systematic uncertainty from the choice of OMP gives an overall uncertainty in C^2 of 12%. The ANC for the ground state was found to be $C^2_{2s1/2} = 1.77 \pm 0.21$ fm^{-1} and for the first excited state $C^2_{1d5/2} = (4.08 \pm 0.49) \times 10^{-3}$ fm^{-1}, consistent with those found from $^{13}\mathrm{C}(^{14}\mathrm{C},^{15}\mathrm{C})^{12}\mathrm{C}$.

C. Summary of the ANC

The ANCs from the two peripheral reactions measured in this work are summarized in Table IV. The average values for the ANC^2 weighted for the uncertainties in the different measurements were 1.88 ± 0.18 fm^{-1} for the ground state and $(4.25 \pm 0.38) \times 10^{-3}$ fm^{-1} for the first excited state. It should be noted that these two reaction measurements have independent, uncorrelated uncertainties (different targets, different beam normalization methods, different methods used to determine optical potentials) up to the use of first-order DWBA reaction theory in the extraction of the ANCs, the contribution from which we do not attempt to estimate. A summary of different determinations of the ANC is given in Table V. An analysis [26] of nuclear breakup measurements of ^{15}C at about 60 MeV/nucleon [31,32] found the $C^2_{2s1/2} = 1.48 \pm 0.18$ fm^{-1} and the analysis of Coulomb dissociation of ^{15}C [33] found $C^2_{2s1/2} = 1.64 \pm 0.03$ fm^{-1}; however, this value was revised to be $C^2_{2s1/2} = 1.74 \pm 0.11$ fm^{-1} in a subsequent erratum [29]. The analysis of a recent measurement of $^{14}\mathrm{C}(d,p)$ at $E_d = 17$ MeV made at the Nuclear Physics Institute of the Czech Academy of Sciences [30] yielded a value of $C^2_{2s1/2} = 1.64 \pm 0.26$ fm^{-1} for the ground state. This smaller value combined with that obtained in this work reconciles what had been a significant difference between the ANC obtained from transfer [28] and those from other methods (breakup [26], Coulomb dissociation [33], and mirror symmetry [27]).

TABLE III. C^2 values from $d(^{14}\mathrm{C},p)^{15}\mathrm{C}$.

	$C^2_{2s1/2}$ (fm^{-1})	$C^2_{1d5/2}$ (fm^{-1})
CH89	1.95	4.22×10^{-3}
KD03	1.59	3.94×10^{-3}
Average	1.77	4.08×10^{-3}

TABLE IV. Summary of squared ANCs found in the different measurements presented in this work.

Experiment	$C^2_{2s1/2}$ (fm^{-1})	$C^2_{1d5/2}$ (fm^{-1})
HI transfer	2.09 ± 0.29	$(4.48 \pm 0.58) \times 10^{-3}$
$d(^{14}\mathrm{C},p)^{15}\mathrm{C}$	1.77 ± 0.21	$(4.08 \pm 0.49) \times 10^{-3}$
Average	1.88 ± 0.18	$(4.25 \pm 0.38) \times 10^{-3}$

III. EVALUATION OF THE SF FROM THE ANC

A 60-MeV total deuteron energy beam from the K500 cyclotron at TAMU-CI was used to measure the forward kinematics (d,p) reaction on a ^{14}C target. Reaction products were again measured using the MDM spectrometer and the Oxford detector as in $^{13}\mathrm{C}(^{14}\mathrm{C},^{15}\mathrm{C})^{12}\mathrm{C}$. In an attempt to compensate for the higher energy and low Z, the pressure in the detector was increased, however, the energy-loss signals were still too small to be of use in particle identification, so instead a thick (1.5″) scintillator after the gas was used to stop both deuterons and protons. Because the higher-energy protons travel much further in the scintillator than the inelastic deuterons of the same rigidity, a good separation was made (Fig. 7). The target was 355 ± 25 μg/cm^2 enriched (∼89%) ^{14}C. Elastic scattering was measured from 3° to 35° laboratory (3.4° to 39.9° c.m.) and the transfer reaction was measured from 3° to 23° laboratory (3.4° to 25.3° c.m.). Elastic scattering and (d,p) reaction products were also measured on a $^{\mathrm{nat}}$C target of known thickness which was compared with the $^{12}\mathrm{C}(d,p)^{13}\mathrm{C}$

TABLE V. Comparison of squared ANC values from previous determinations.

Reference	$C^2_{2s1/2}$ (fm^{-1})	$C^2_{1d5/2}$ (fm^{-1})
[26]	1.48 ± 0.18	
[27]	1.89 ± 0.11	
[28]	2.14	
[29]	1.74 ± 0.11	
[30]	1.64 ± 0.26	$(3.55 \pm 0.43) \times 10^{-3}$
This work	1.88 ± 0.18	$(4.25 \pm 0.38) \times 10^{-3}$

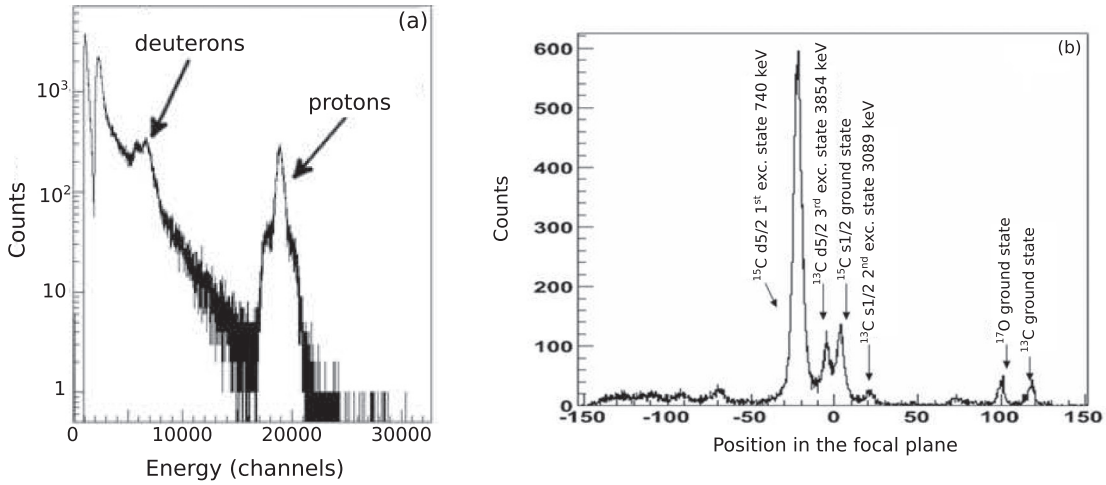

FIG. 7. Particle identification from the ^{14}C$(d,p)^{15}$C reaction. In (a) a good separation of protons from inelastically scattered deuterons is shown. Panel (b) shows the contents of the proton peak plotted as a function of position in the focal plane.

that occurred on the ^{12}C impurity in the ^{14}C target to determine the ^{12}C content ($\sim$11%).

As in the case of the inverse kinematics $d(^{14}\mathrm{C},p)^{15}\mathrm{C}$ reaction described previously, the angular distribution was calculated using the ADWA and the code FRESCO. The results of these calculations and the measured angular distributions are shown in Fig. 8. The optical potential in the entrance channel was given by the sum of the single nucleon potentials of the incident proton and neutron evaluated at half the deuteron energy. The potentials were obtained from the KD03 global parametrization. Because this was intended to be a nonperipheral reaction that could be used to determine the SF with the method of Ref. [11], this calculation of the cross section was repeated for a variety of choices of binding potential geometry by varying the radius parameter (r_0) of the WS binding potential, while keeping the diffuseness fixed. The depth was adjusted for each point to reproduce the neutron separation energy. For a peripheral reaction the dependence on the binding potential geometry [and thus on the single-particle ANC (SPANC)] will be weak and one can then determine the ANC. If, however, the dependence is strong, one can compare this calculation with experiment and find a particular range of SPANC values that produce the correct ANC and then use this to determine the SF.

Following Ref. [11], a function

$$R^{\mathrm{DW}}(b_{nlj}) = \left| \frac{\tilde{T}_{\mathrm{int}}}{b_{nlj}} + \tilde{T}_{\mathrm{ext}} \right|^2 \tag{9}$$

was constructed, where the single-particle ANC, b_{nlj}, is a function of the binding potential geometry and $\tilde{T}_{\mathrm{int}}$ and $\tilde{T}_{\mathrm{ext}}$ are the transfer matrix elements representing integration over the interior and exterior regions, respectively, as described in Ref. [11]. The experimental counterpart of Eq. (9) is

$$R^{\mathrm{exp}} = \frac{\frac{d\sigma}{d\Omega}^{\mathrm{exp}}}{C_{lj}^2}, \tag{10}$$

where C_{lj}^2 is the ANC squared. These functions were compared for the angle corresponding to the most forward point measured in the experiment and are summarized in Fig. 9.

The equality $R^{\mathrm{exp}} = R^{\mathrm{DW}}(b_{nlj})$ should allow us to determine the SPANC given the additional condition that the

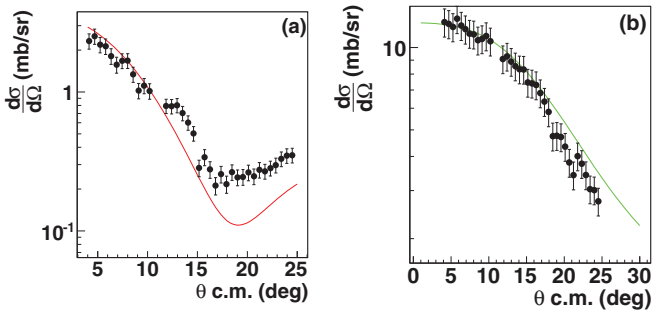

FIG. 8. (Color online) Shown in (a) is the angular distribution for ^{14}C$(d,p)^{15}$C ($E_d = 60$ MeV) transfer to the ground state (black dots) and the ADWA calculation (red); the same is shown in (b) for transfer to the $1d_{5/2}$ excited state (black dots, experiment; green line, ADWA).

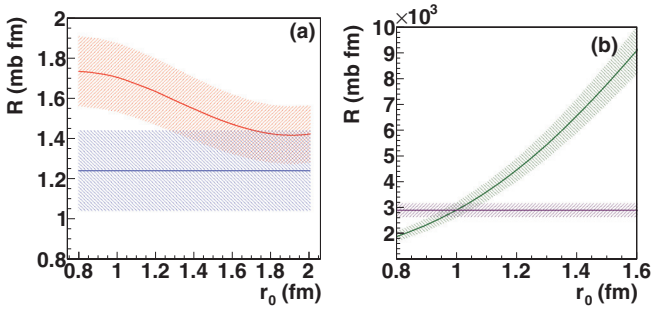

FIG. 9. (Color online) R_{DW} (red, curved line) and R_{exp} (blue, horizontal line) for ^{14}C$(d,p)^{15}$C ($E_d = 60$ MeV) transfer to the ground state (a) and the $d_{5/2}$ first excited state (R_{DW}, green curved line; R_{exp}, purple horizontal line) (b) as a function of the radius parameter, r_0, of the WS binding potential. The uncertainties are shown by the hatched areas. In the calculation this is taken to be 10% and reflects the systematic uncertainty.

normalization of the external contribution to the reaction amplitude is fixed correctly via the ANC. However, the ground-state $R^{\mathrm{DW}}(b_{nlj})$ shows a relatively weak dependence on the SPANC, that is, on the geometry of the single-particle neutron bound-state potential in ^{15}C. This is a sign that the internal contribution T_{int}/b_{nlj} is either small or has little dependence on the SPANC. From Fig. 14 (see below) we can see that the internal contribution, which is determined by the post-ADWA cross section (black solid line) at $R_{nA} \approx 6.5$ fm (at this channel radius the surface part reaches its maximum), is quite large. Hence, the weak dependence of $R^{\mathrm{DW}}(b_{nlj})$ is the result of the weak dependence on b_{nlj} of the internal part T_{int}/b_{nlj} and we cannot reliably determine the SPANC at which $R^{\mathrm{exp}} = R^{\mathrm{DW}}(b_{nlj})$. Based on the divergence around $r_0 = 1.25$ fm, this gives an upper limit for the SF for transfer to the ground state of 0.93.

This is a very instructive case. If we use the standard procedure for determining the SF from the experimental data and we adopt a standard set of geometrical parameters such as $r_0 = 1.25$ fm and $a = 0.65$ fm, we find $b_{nlj} = 1.42$ fm$^{-1/2}$ and SF $\mathrm{SF}_{nlj} = 0.70$, which follows by comparing the data to the normalization of the ADWA calculated differential cross section. Using the equation

$$C_{lj}^2 = \mathrm{SF}_{nlj} b_{nlj}^2, \tag{11}$$

we get for the ANC $C_{lj}^2 = 1.41$ fm^{-1}. However, we can equally well use a higher r_0 or a that leads to a larger b_{nlj} and smaller SFs. For $b_{nlj} < 1.42$ fm$^{-1/2}$ the obtained ANCs will be smaller than the experimental ANC, while at $b_{nlj} > 1.42$ fm$^{-1/2}$ the ANCs will agree with the experimentally determined ANC within experimental uncertainties.

Our inability to pinpoint the SPANC and, consequently, the SF from the transfer reaction data at 60 MeV, with the external contribution fixed via the ANC, reflects the fact that transfer reactions do not always present a proper tool to determine the SF, and additional information about the geometry of the single-particle potential is needed. An additional problem in using the ANC-based method of determination of the SF is caused by a strong sensitivity of the analysis to the deuteron optical potential. For example, if we would use only the KD03 global optical potential parameters, the experimentally determined ANC would be lower and, correspondingly, R^{exp} would be higher, better overlapping with the theoretical $R^{\mathrm{DW}}(b_{nlj})$. Note that there are no single-nucleon optical potentials available in literature for scattering on light nuclei such as ^{14}C. These are needed to calculate the deuteron optical potential at 60 MeV in the entrance channel and the proton optical potential in the exit channel. Both of the optical potentials used, CH89 and KD03, are not fitted to analyze our data and the lack of reliable nucleon optical potentials is another reason for the failure of the ANC-based method. Finally, in contrast to the standard approach, in which the inaccuracy of the single-particle approach in the nuclear interior is compensated by arbitrary variation of the external part (the information about the ANC is disregarded), the ANC-based method, *a priori*, requires a more accurate treatment of the nuclear interior because the external contribution is fixed and the main model dependence comes from the nuclear interior part.

While Fig. 9 shows that the ground-state dependence of the calculated cross section on the binding potential geometry is weak, a stronger dependence on the binding potential geometry is observed for the transfer to the first excited state. As seen on the right in Fig. 9, $R^{\mathrm{DW}}(b_{nlj})$ overlaps with R^{exp} over the range of r_0 from around 0.91 to 1.08 fm. From the SPANC values for those radius parameters and Eq. (11), we get a range of SF values from 1.62 to 1.18, which is considerably higher than expected and also higher than that obtained by mirror-symmetry considerations with ^{15}F. Thus, in this case, despite a sharp dependence of $R^{\mathrm{DW}}(b_{nlj})$ on the SPANC b_{nlj}, we cannot reconcile the ANC and SF. Once again, the ANC-based method reveals shortcomings of the standard approach. If we would use a conventional approach with the standard geometry $r_0 = 1.25$ fm and $a = 0.65$ fm, we get the SPANC $b_{nlj} = 1.42$ and the SF $\mathrm{SF}_{nlj} = 0.70$. It leads to $C_{lj}^2 = 1.41$ fm^{-1}, which is significantly lower than the experimental ANC squared. This clearly shows that the single-particle approach in the nuclear interior should be improved by a more microscopic approach. Also, the ambiguity in the optical potentials contribute to the problem.

While Fig. 9 shows that the ground-state dependence of the calculated cross section on the binding potential geometry is weak, a stronger dependence on the binding potential geometry is observed for the transfer to the first excited state. As seen in (b) in Fig. 9, R_{calc} overlaps with R_{exp} over the range r_0 from around 0.91 to 1.08 fm. From the single-particle ANC values for those radius parameters and the relation

$$\mathrm{SF}_{lj} = \frac{C_{lj}^2}{b_{nlj}^2} \tag{12}$$

we get a range of SF values from 1.62 to 1.18, which is considerably higher than expected and also higher than that obtained by mirror-symmetry considerations with ^{15}F which are discussed in the following section. This indicates that the interior contribution to the transfer matrix element is not being correctly calculated and that a more sophisticated microscopic approach needs to be developed. The difficulty in correctly calculating this interior portion combined with the fact that most transfer reactions are dominated by peripheral and surface components highlights the difficulty in determining spectroscopic factors by means of transfer reactions.

IV. STUDY OF THE ^{15}C SF VIA THE MIRROR NUCLEUS, ^{15}F

In this section we use the ^{15}C-^{15}F mirror symmetry to obtain a restriction on the SF of the two lowest states in these nuclei. Specifically, we use the fact of near equidistant level spacing in mirror nuclei with the exclusion of the abnormally large isotopic shift of the S states which is known as the Nolen Shiffer effect [34]. The ^{15}C-^{15}F case has been the topic of many investigations. The most detailed and most recent studies were made by Fortune [35] and Fortune and Sherr [36,37], who used the isospin conservation and shell-model corrections to find the isotopic shifts of the levels in question. A comprehensive

review of the properties of the unstable light nuclei was made by Millener [38]. Our approach is different from the others in that, on the basis of the previous results, (a) we assume that the single-particle wave functions generated by the Woods-Saxon potential are good approximations for the structure of the states [30,34–38], and (b) we fit experimental data on the levels in question with the aim to fix the potential parameters. The potential parameters then can be used further to obtain the SF and the ANC. The neutron binding energies (BEs) for the ground $(1/2+)$ and the first excited $(5/2+)$ states in ^{15}C are well known to be 1.218 and 0.478 MeV, respectively. The compilation of data for the two lowest states in ^{15}F can be found in Ref. [35]. We averaged these data to obtain the BE of the proton for the ground state in ^{15}F as 1370 ± 70 keV with a width of 750 ± 100 keV, and for the $5/2+$ first excited state -2780 ± 40 keV with a width of 275 ± 40 keV [39].

In these calculations, we fixed the Coulomb potential as the potential of a uniformly charged sphere with the $R_C = 1.45 \times 14^{1/3}$ fm. Large R_C provides for an agreement with the rms radius of the charge distribution in ^{16}O. The parameters of the Woods-Saxon potential were varied over $1.1 < r_0 < 2.2$ fm and $0.55 < a < 0.72$ fm. For each combination of r_0 and a, the depth of the real potential was fixed by a requirement to fit BE of the neutron in ^{15}C. Also, the conventional spin-orbital potential with fixed parameters of $V_{so} = 6.4$ MeV and $a = 0.64$ fm was used in the calculations of the BE for the $5/2+$ state. We observed that 10% variations in the spin-orbit potential did not influence our results.

The fit for the levels in ^{15}C having been obtained, calculations were made for ^{15}F with the same parameters but taking into account the Coulomb interaction with the extra proton. Figure 10 presents dependence of the BE (which is negative) of the proton in the ^{15}F $5/2+$ state versus the rms radius of the mirror state in ^{15}C. It is seen that the larger the rms radius, the more stable the mirror state in ^{15}F. The dependence is easily understood as a result of an effective decrease in

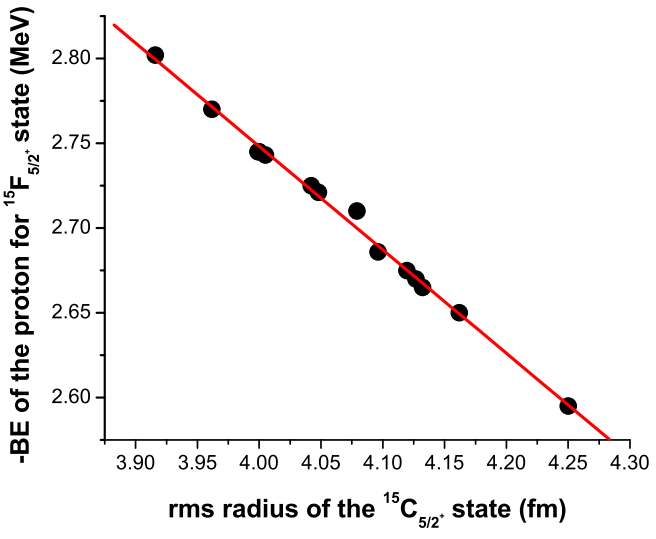

FIG. 10. (Color online) The (negative) proton binding energy for the $5/2+$ state in ^{15}F versus the rms radius of the mirror state in ^{15}C generated by different parameters of the Woods-Saxon potential.

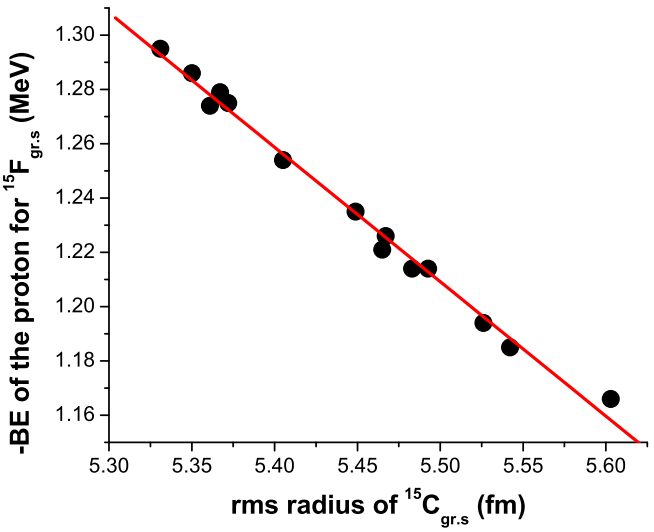

FIG. 11. (Color online) The same as Fig. 10 for the $1/2+$ ground state in ^{15}F.

the Coulomb potential for larger radii of the wave functions. There is a very small spread of points relative to the general trend, which tells us that the specific values of r_0 and a are not important, but their combination affecting the value of the rms radius is important. As is seen in Fig. 10, the experimental BE corresponds to the rms radius of 3.97 fm. Because the proton BE in the $5/2+$ state should not depend upon the small corrections to the single-particle wave function, this result defines the geometry of the potential. This makes a restriction on $r_0 + a = 1.78 \pm 0.05$ fm.

Figure 11 presents a similar graph for the ^{15}C-^{15}F ground states. A trend similar to that in Fig. 10 is evident. However, the spread of the points is slightly larger than in Fig. 10. The points which are above of the curve correspond to a lower a/r_0 ratio.

The geometry of the potential having been fixed by the $5/2+$ analysis, this geometry was then used to calculate the BE of the proton in the ground state of ^{15}F, which was found to be 1.295 ± 25 keV. Any corrections to the pure $2s$ structure of this state should push it up (increasing instability of ^{15}F). For example, if the ground state of ^{15}C were an $l = 2$ state, then the mirror state in ^{15}F would be unbound to proton decay by 2.119 MeV. Hence, if the $l = 0$ configuration were absent in the ^{15}C-^{15}F ground states, the BE difference between the ground and the first excited states in ^{15}F would be $2780 - 2119 = 661$ keV. If the ground state were a 100% pure $2s$ single-particle state, the difference would be $2780 - 1295 = 1495$ keV [the electromagnetic spin-orbital interaction ($\sim$30 keV) should be added to make the difference 1525 keV]. Making the needed proportions and taking into account the experimental BE for the ^{15}F ground state (1370 keV) and the uncertainties, we obtain $\mathrm{SF}_{gs} = 0.91^{+0.09}_{-0.09}$.

Next we consider the restrictions on the SF by the widths of the states in ^{15}F,

$$\mathrm{SF} = \frac{\Gamma}{\Gamma_{s.p.}} \tag{13}$$

The SF is the ratio of the experimentally determined width of the state to the width calculated using shell-model wave functions. It is known that the most sophisticated way to calculate widths of broad states is to consider a pole in a complex plane [40]. Here we used the dependence of the maximum of the wave function upon the BE, as this method also gives close results [40]. Moreover, this approach was used to fit the experimental data [41,42]. The calculated widths with parameters $r_0 = 1.18$ and $a = 0.6$ are 0.590 MeV (for the ground state) and 230 keV (for the $5/2+$ state in ^{15}F). After correcting the calculated ground-state width to reproduce the experimental BE, it becomes 720 keV. The calculated values are still smaller than the experimental ones. Taking into account the experimental uncertainties in the widths and the excitation energies, we obtain for the ground state $\mathrm{SF_{gs}} \leqslant 0.90$, and for the first excited state $\mathrm{SF_{exc.}} \leqslant 0.93$. We tested and subsequently neglected the weak dependence (15 keV for the excited state) of the penetrability on the specific values of r_0 and a.

If we use the the single-particle potential parameters adopted here and the $\mathrm{SF_{gs}} \leqslant 0.90$ we obtain the ANC values $C^2_{\mathrm{gs}} \leqslant 1.66$, which are lower than the values found from transfer reactions presented in this work. This inconsistency once again demonstrates that if we fix the external contribution using the ANC, a standard single-particle approach used to calculate the internal contribution is not accurate.

Very general considerations will result in the expectation of a larger distortion of the simple single-particle configuration for the excited $(5/2+)$ state than for the ground state. As was presented in Ref. [37], it is not surprising that the admixture is larger for the $5/2+$ state, because $s_{1/2}$ lies below $d_{5/2}$ and $2+ \otimes d$ lies above $2+ \otimes s$, so that the unperturbed $5/2+$ states will be closer together than the $1/2+$ ones increasing the mixing for $5/2+$.

V. NEW INSIGHT INTO DEUTERON STRIPPING THEORY

To better understand the peripheral nature of the higher-energy (d,p) reaction and the failure of the new method described in Sec. III, an examination of the underlying DWBA reaction theory is needed. In Ref. [43] a new theory of the deuteron stripping reactions populating bound states and resonances was developed. It combines the surface integral formalism [44,45], the R-matrix method, and the CDCC method. While the work on the code of the new approach is in progress, here we demonstrate the new theory using the DWBA.

Let us consider the deuteron stripping reaction to bound states,

$$d + A \to p + F, \tag{14}$$

where $F = (A\,n)$ is the bound state.

The post form of the DWBA amplitude is given by

$$M^{\mathrm{DW(post)}}(\mathbf{k}_{pF}, \mathbf{k}_{dA}) = \langle \Phi_f^{(-)} | \Delta\, V_{pF} | \Phi_i^{(+)} \rangle, \tag{15}$$

where $\Phi_i^{(+)} = \varphi_{pn}\chi_{dA}$ and $\Phi_f^{(-)} = I_A^F \chi_{pF}^{(-)}$ are the initial and final channel wave functions, φ_{pn} is the deuteron bound-state wave function, $\chi_{dA}^{(+)} \equiv \chi_{\mathbf{k}_{dA}}^{(+)}$ and $\chi_{pF}^{(-)} \equiv \chi_{\mathbf{k}_{pF}}^{(-)}$ are the distorted waves in the initial and final channels, $\mathbf{k}_{ij}$ is the relative momentum of particles i and j,

$$I_A^F(\mathbf{r}_{nA}) = \sqrt{A+1}\{\langle \varphi_A(\zeta_A) | \varphi_F(\zeta_A; \mathbf{r}_{nA}) \rangle\} \tag{16}$$

is the overlap function of the bound-state wave functions $\varphi_F(\zeta_A; \mathbf{r}_{nA})$ and $\varphi_A(\zeta_A)$ of nuclei F and A, correspondingly, $\mathbf{r}_{nA}$ is the radius-vector connecting n and the center of mass of A. The integration in Eq. (16) is taken over all the internal coordinates ζ_A of nucleus A, which include also spin-isospin ones. The factor $\sqrt{A+1}$ is the result of the antisymmetrization in the isospin formalism between the transferred neutron and nucleons of nucleus A. Also, $\Delta V_{pF} = U_{pA} + V_{pn} - U_{pF}$ is the transition operator in the post form, U_{ij} is the optical potential describing the interaction between nuclei i and j, and V_{pn} is the p-n interaction potential. Note that in a standard DWBA the overlap function is approximated by

$$I_A^F(\mathbf{r}_{nA}) = S_{nA}\, \varphi_n(\mathbf{r}_{nA}), \tag{17}$$

where S_{nA} is the spectroscopic factor of the configuration $n + A$ in F and φ_n is the neutron bound-state wave function in nucleus F calculated in the adopted mean-field potential. However, here we keep the overlap function rather than using approximation (17).

Similarly, the prior form of the DWBA amplitude is given by

$$M^{\mathrm{DW(prior)}}(\mathbf{k}_{pF}, \mathbf{k}_{dA}) = \langle \Phi_f^{(-)} | \Delta\, V_{dA} | \Phi_i^{(+)} \rangle, \tag{18}$$

where $\Delta V_{dA} = U_{pA} + U_{nA} - U_{dA}$.

The matrix element of the DWBA reaction amplitude can be expressed in terms of the integrals over two Jacobian variables $\mathbf{r}_{pF}$ and $\mathbf{r}_{nA}$. One of the main goals of measuring transfer reactions (14) is to determine the overlap function $I_A^F(\mathbf{r}_{nA})$. In a new approach the integral over $\mathbf{r}_{nA}$ is divided into the internal ($r_{nA} \leqslant R_{nA}$) and external ($r_{nA} > R_{nA}$) parts, where R_{nA} is the channel radius. After that, using the surface integral formalism both post and prior forms can be written as [43])

$$\begin{aligned} M^{\mathrm{DW(post)}}(\mathbf{k}_{pF}, \mathbf{k}_{dA}) &= M^{\mathrm{DW(prior)}}(\mathbf{k}_{pF}, \mathbf{k}_{dA}) \\ &= M_{\mathrm{int}}^{\mathrm{DW(post)}}(\mathbf{k}_{pF}, \mathbf{k}_{dA}) \\ &\quad + M_S^{\mathrm{DW}}(\mathbf{k}_{pF}, \mathbf{k}_{dA}) \\ &\quad + M_{\mathrm{ext}}^{\mathrm{DW(prior)}}(\mathbf{k}_{pF}, \mathbf{k}_{dA}). \end{aligned} \tag{19}$$

Here

$$M_{\mathrm{int}}^{\mathrm{DW(post)}}(\mathbf{k}_{pF}, \mathbf{k}_{dA}) = \langle \Phi_f^{(-)} | \Delta\, V_{pF} | \Phi_i^{(+)} \rangle|_{r_{nA} \leqslant R_{nA}} \tag{20}$$

is the internal DWBA post-form amplitude, in which the integration over r_{nA} is taken in the subspace $r_{nA} \leqslant R_{nA}$, while the integration over r_{pF} is performed over the whole space;

$$M_{\mathrm{ext}}^{\mathrm{DW(prior)}}(\mathbf{k}_{pF}, \mathbf{k}_{dA}) = \langle \Phi_f^{(-)} | \Delta_{V_{dA}} | \Phi_i^{(+)} \rangle|_{r_{nA} > R_{nA}} \tag{21}$$

is the external prior form of the DWBA amplitude, in which the integration over r_{nA} is taken in the subspace $r_{nA} > R_{nA}$, while the integration over r_{pF} is performed over the whole space. It is clear that when R_{nA} increases $M_{\mathrm{int}}^{\mathrm{DW(post)}} \to M^{\mathrm{DW(post)}}$, while when $R_{nA} \to 0$ $M_{\mathrm{ext}}^{\mathrm{DW(prior)}} \to M^{\mathrm{DW(prior)}}$, where always $M^{\mathrm{DW(post)}} = M^{\mathrm{DW(prior)}}$. Finally, M_S^{DW} is the surface amplitude, which is given by the surface integral in the subspace over $\mathbf{r}_{nA}$ at $r_{nA} = R_{nA}$ while the integration over $\mathbf{r}_{pF}$ is performed over

the whole space:

$$M_S^{\rm DW}(\mathbf{k}_{pF},\mathbf{k}_{dA}) = \frac{1}{2\,\mu_{nA}}\,R_{nA}^2\int d\,\mathbf{r}_{pF}\,\chi^{(+)}_{-\mathbf{k}_{pF}}(\mathbf{r}_{pF}) \times \int d\,\Omega_{\mathbf{r}_{nA}}\left\{\varphi_{pn}(r_{pn})\,\chi^{(+)}_{\mathbf{k}_{dA}}(\mathbf{r}_{dA}) \times \frac{\partial\left[I_A^F(\mathbf{r}_{nA})\right]^*}{\partial\, r_{nA}} - \left[I_A^F(\mathbf{r}_{nA})\right]^* \times \frac{\partial\,\varphi_{pn}(r_{pn})\,\chi^{(+)}_{\mathbf{k}_{dA}}(\mathbf{r}_{dA})}{\partial\, r_{nA}}\right\}\Big|_{r_{nA}=R_{nA}}. \quad (22)$$

Here we took into account that $\chi^{(-)*}_{\mathbf{k}}(\mathbf{r}) = \chi^{(+)}_{-\mathbf{k}}(\mathbf{r})$.

Representation of the post and prior amplitudes in form (19) has the following advantages:

(i) It shows explicitly that both amplitudes do coincide;
(ii) it allows one to determine the channel radius as the radius R_{nA} at which the surface amplitude reaches its maximum value;
(iii) it allows one to determine how peripheral a reaction is by estimating the internal part contribution, which is given by $M_{\rm int}^{\rm DW(post)}(\mathbf{k}_{pF},\mathbf{k}_{dA})$.

Note that the main goal of Ref. [43] was to apply the surface integral formalism for the CDCC method. Because the corresponding code is not yet available, we calculate here the differential cross section obtained from the amplitude (19). However, for the entry channel optical potential we use the adiabatic model prescription [22], in which the $d-A$ optical potential in the initial state is given by the sum of the proton and neutron optical potentials calculated at half deuteron energy at the distance $r_{pA} = r_{nA} = r_{dA}$. We use the full transition operator in the post and prior forms rather than just V_{pn} potential. Each nucleon optical potential in the entry channel and the proton optical potential in the exit channel is taken in the Koning and Delaroche form [24].

Despite the fact that both post and prior form DWBA amplitudes coincide, their behaviors as functions of R_{nA} are quite different and actually they coincide only at large-enough R_{nA}. In Figs. 12–15 we demonstrate the behavior of each cross section generated by the corresponding amplitude of the right-hand side of Eq. (19).

All four figures are very instructive. We see that at large R_{nA} post- and prior-form cross sections coincide, as they should. The radius R_{nA} at which the surface integral reaches maximum is actually the channel radius $R_{\rm max}$. For the ^{14}C$(d,p)^{15}$C$(2s_{1/2};\ E_x = 0.0$ MeV) reaction at 23.4 MeV (Fig. 12) $R_{\rm max} = 4.70$ fm, while for the ^{14}C$(d,p)^{15}$C$(1d_{5/2};\ E_x = 0.7$ MeV) reaction at 23.4 MeV (Fig. 13) $R_{\rm max} = 5.0$ fm. In both cases, the contribution of the internal part (black solid line) at the channel radius $R_{\rm max}$ is significantly smaller than the surface (dashed blue line) and the external part [prior form (red dotted line) integrated for $r_{nA} \geqslant R_{nA}$]; that is, both reactions are peripheral.

We see a different pattern for the 60-MeV deuteron energy. For the reaction ^{14}C$(d,p)^{15}$C$(2s_{1/2};\ E_x = 0.0$ MeV) at $E_d = 60.0$ MeV (Fig. 14), the channel radius $R_{\rm max} = 6.0$ fm and the contribution of the nuclear interior is significantly larger than the surface and external terms; that is, this reaction is not peripheral. For the transition to excited state at $E_d = 60$ MeV (Fig. 15) the channel radius $R_{\rm max} = 4$ fm is smaller, but at this channel radius the internal contribution is also small, although not negligible.

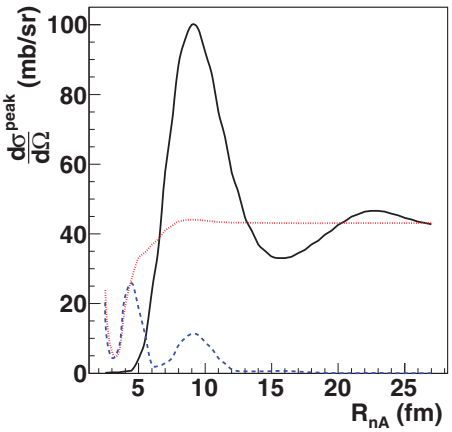

FIG. 12. (Color online) Differential cross section dependence on R_{nA}, where $A = {}^{14}$C, for the reaction ^{14}C$(d,p)^{15}$C$(2s_{1/2};\ E_x = 0.0$ MeV) at the incident deuteron energy of 23.4 MeV. Each cross section is calculated using the full transition operator and the adiabatic model prescription for the deuteron optical potential. The black solid line is the post form of the ADWA differential cross section calculated using the amplitude given by Eq. (20); the red dotted line is the prior form of the ADWA differential cross section calculated using the amplitude given by Eq. (18) with integration over r_{nA} taken from 0 to R_{nA}; the blue dashed line is the ADWA differential cross section calculated using the surface amplitude $M_S^{\rm DW}$ [43].

VI. ASTROPHYSICAL ^{14}C$(n,\gamma)^{15}$C REACTION RATE

The radiative neutron capture rates for ^{14}C$(n,\gamma)^{15}$C have been calculated using the code RADCAP [46] and the ANCs that

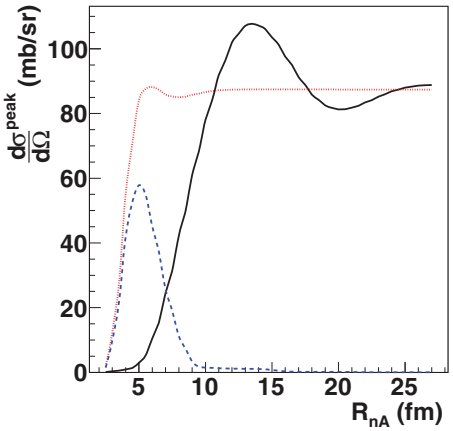

FIG. 13. (Color online) Differential cross section dependence on R_{nA} for the reaction ^{14}C$(d,p)^{15}$C$(1d_{5/2};\ E_x = 0.7$ MeV) at the incident deuteron energy of 23.4 MeV. Other notations are the same as in Fig. 12.

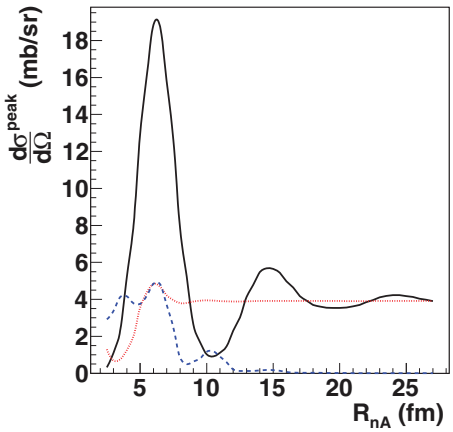

FIG. 14. (Color online) Differential cross section dependence on R_{nA} for the reaction ^{14}C$(d,p)^{15}$C$(2s_{1/2}$; $E_x = 0.0$ MeV) at the incident deuteron energy of 60.0 MeV. Other notations are the same as in Fig. 12.

were found in this work. At astrophysical energies only the first two states, the $2s_{1/2}$ ground state and the 740-keV $1d_{5/2}$ first excited state, contribute to the neutron capture cross section. The next state at 3.1 MeV and ~40 keV in width is too high to contribute [47]. S-wave neutron capture is not significant for the ^{14}C(n,γ) reaction owing to parity conservation [7]. ^{14}C has $J^\pi = 0^+$ and coupled with an s-wave neutron would give a system with $J^\pi = 1/2^+$. Because the ground and first excited states in ^{15}C are $J^\pi = 1/2^+$ and $J^\pi = 5/2^+$, respectively, this only allows for weak $M1$ and $E2$ transitions. Alternatively, a p-wave neutron would give the $^{14}\mathrm{C} + n$ system $J^\pi = 1/2^-$ or $3/2^-$, which would then be able to allow $E1$ transitions and thus a much higher cross section. For the first excited state, $E2$ transitions should also be taken into account [7].

The neutron binding potential used was of the WS form with the real potential depth adjusted to reproduce the neutron BE for each state. The binding potential parameters were, for the

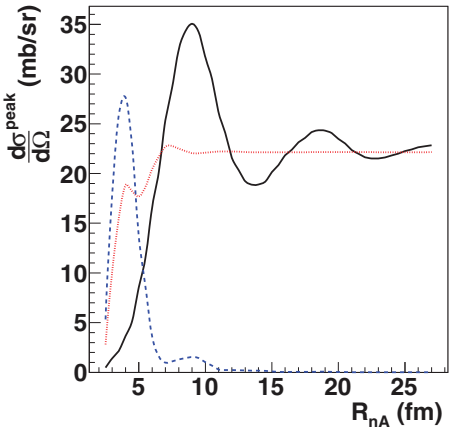

FIG. 15. (Color online) Differential cross section dependence on R_{nA} for the reaction ^{14}C$(d,p)^{15}$C$(1d_{5/2}$; $E_x = 0.7$ MeV) at the incident deuteron energy of 60.0 MeV. Other notations are the same as in Fig. 12.

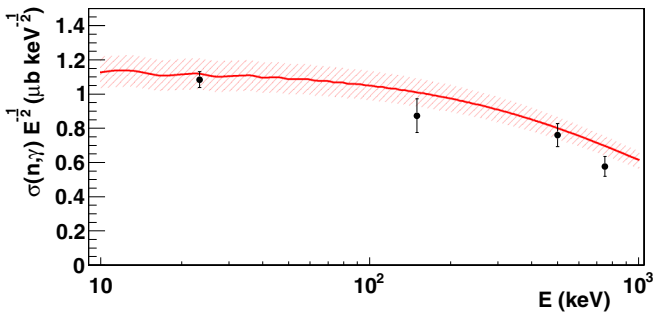

FIG. 16. (Color online) Calculated cross section (sum of capture to gs and first excited state, red line with red uncertainty) compared with Ref. [5] (black dots).

ground state, $V_0 = -54.71$ MeV, $r = 2.89$ fm, $a = 0.60$ fm, and $V_{SO} = -9.30$ MeV (using the SO convention described in Ref. [46]). The same geometry was used for the central and SO parts of the potential. The central depth was $V_0 = -54.11$ MeV for the first excited state.

The cross section divided by the square root of the energy is given in Fig. 16 for both capture to the ground state and the first excited state. The capture to the first excited-state accounts for about 4% of the total (only the first two states are considered). The sum of the results for the rates for two states is shown along with the recent direct measurement of Reifarth *et al.* [5] in Fig. 16. The calculated value for the cross section for capture to the ground state at $E_{\mathrm{c.m.}} = 23$ keV was $\sigma_{\mathrm{gs}}(23\ \mathrm{keV}) = 5.1 \pm 0.4\ \mu$b and to the first excited state was $\sigma_{\mathrm{exc}}(23\ \mathrm{keV}) = 0.22 \pm 0.02\ \mu$b. The total cross section at 23 keV was found to be $\sigma(23\ \mathrm{keV}) = 5.4 \pm 0.5\ \mu$b, which is in good agreement with the most recent direct measurement, $\sigma(23\ \mathrm{keV}) = 5.2 \pm 0.3\ \mu$b [5]. In Ref. [33] the value for the differential cross section was obtained by multiplying the Maxwellian average cross section (MACS) reported in Ref. [5] by 0.67, using the assumption of a perfect $E^{-1/2}$ energy dependence, but no explanation was given for why the authors of Ref. [33] chose to eschew the differential cross section presented in Ref. [5] in favor of the simplified normalization of the MACS. Using the value given in Ref. [5] would have resulted a disagreement for the cross section obtained in Ref. [33]; however, given the corrected value in Ref. [29], it would likely agree within the stated uncertainty.

VII. SUMMARY

The ANC for $^{15}\mathrm{C} \leftrightarrow {}^{14}\mathrm{C} + n$ has been determined for the ground state and first excited state of ^{15}C from multiple new reaction measurements. The average values are $C^2_{2s1/2} = 1.88 \pm 0.18$ fm^{-1} for the ground state and $C^2_{1d5/2} = 4.25 \pm 0.38 \times 10^{-3}$ fm^{-1} for the first excited state. This was done as part of an effort to evaluate the new method of Ref. [11] to determine SFs with less uncertainty. The new method was found to produce an upper limit on the SF for the ground state owing to a weak dependence on the neutron binding potential geometry and thus on the interior portion of the transfer matrix element for the nonperipheral reaction measured. An even

less peripheral reaction might yield better results; however, ^{14}C$(d,p)^{15}$C seems to be a poor choice because of the large momentum mismatch and resulting small cross section if this reaction were to be measured at a high-enough energy to have an adequate dependence on the interior. The method gave a range of SF values for the first excited state; however, that range was quite high (SF = 1.18 to 1.62), which does not match with the value of slightly less than 1 expected for a strong single-particle state, nor does it match with the result obtained from mirror-symmetry considerations. The need to have a strong-enough dependence on the interior while at the same time having a reaction that is described well in the DWBA or ADWA is a serious limitation of the method of Ref. [11]. A more microscopic approach to the reaction theory has been presented and future developments in this area may allow a better description of the nuclear interior contribution to the transfer matrix element and thus a better determination of the SF.

Using the ANCs found in the process of evaluating the new method, the astrophysical direct-capture reaction rate of ^{14}C$(n,\gamma)^{15}$C was calculated and the results are in good agreement with the most recent direct measurement.

ACKNOWLEDGMENTS

This work was supported by DOE Office of Nuclear Physics Grant No. DE-FG02-93ER40773, NNSA SSAA Grants No. DE-FG52-09NA29467, No. DE-SC0004958, and No. DE-AC52-07NA27344* (TORUS), the NSF under Grant No. PHY-0852653, and the Welch Foundation. This work was supported in part by UEFISCDI Romania under Programme PN-II Contract No. 55/05.10.2011. This work was also supported by Grant No. LH11001 of the AMVIS Project as part of the Czech-American cooperation (www.amvis.cz).

*with LLNL

[1] R. Malaney and W. Fowler, Astrophys. J. **333**, 14 (1988).
[2] M. Wiescher, J. Görres, and H. Schatz, J. Phys. G: Nucl. Part. Phys. **25**, R133 (1999).
[3] M. Terasawa, K. Sumiyoshi, T. Kajino, G. Mathews, and I. Tanihata, Astrophys. J. **562**, 470 (2001).
[4] H. Beer, M. Wiescher, F. Käppeler, J. Görres, and P. Koehler, Astrophys. J. **387**, 258 (1992).
[5] R. Reifarth, M. Heil, C. Forssen, U. Besserer, A. Couture *et al.*, Phys. Rev. C **77**, 015804 (2008).
[6] A. Mukhamedzhanov, H. L. Clark, C. Gagliardi, Y.-W. Lui, L. Trache *et al.*, Phys. Rev. C **56**, 1302 (1997).
[7] M. Wiescher, J. Görres, and F. Thielemann, Astrophys. J. **363**, 340 (1990).
[8] J. Lee, J. A. Tostevin, B. A. Brown, F. Delaunay, W. G. Lynch, M. J. Saelim, and M. B. Tsang, Phys. Rev. C **73**, 044608 (2006).
[9] M. B. Tsang, J. Lee, S. C. Su, J. Y. Dai, M. Horoi, H. Liu, W. G. Lynch, and S. Warren, Phys. Rev. Lett. **102**, 062501 (2009).
[10] A. M. Mukhamedzhanov, F. M. Nunes, and P. Mohr, Phys. Rev. C **77**, 051601 (2008).
[11] A. M. Mukhamedzhanov and F. M. Nunes, Phys. Rev. C **72**, 017602 (2005).
[12] L. Trache, A. Azhari, H. L. Clark, C. A. Gagliardi, Y.-W. Lui, A. M. Mukhamedzhanov, R. E. Tribble, and F. Carstoiu, Phys. Rev. C **61**, 024612 (2000).
[13] D. Youngblood and J. Bronson, Nucl. Instrum. Methods Phys. Res., Sect. A **361**, 37 (1995).
[14] D. M. Pringle, W. N. Catford, J. S. Winfield, D. G. Lewis, N. A. Jelley, and K. W. Allen, Nucl. Instrum. Methods Phys. Res., Sect. A **245**, 230 (1986).
[15] J. S. Winfield, D. M. Pringle, W. N. Catford, D. G. Lewis, N. A. Jelley, and K. W. Allen, Nucl. Instrum. Methods Phys. Res., Sect. A **251**, 297 (1986).
[16] A. M. Mukhamedzhanov, C. A. Gagliardi, and R. E. Tribble, Phys. Rev. C **63**, 024612 (2001).
[17] T. Al-Abdullah, F. Carstoiu, X. Chen, H. L. Clark, C. Fu *et al.*, Phys. Rev. C **81**, 035802 (2010).
[18] M. Rhoades-Brown, S. Pieper, and M. Macfarlane, Computer code PTOLEMY, Argonne National Lab Report No. ANL-76-11-rev-1, 1978.
[19] Evaluated nuclear structure data file (ENSDF), http://www.nndc.bnl.gov/ensdf/
[20] B. T. Roeder, M. McCleskey, L. Trache, A. A. Alharbi, A. Banu *et al.*, Nucl. Instrum. Methods Phys. Res., Sect. A **634**, 71 (2011).
[21] I. J. Thompson, Comput. Phys. Rep. **7**, 167 (1988).
[22] R. C. Johnson and P. J. R. Soper, Phys. Rev. C **1**, 976 (1970).
[23] R. L. Varner, Phys. Rep. **201**, 57 (1991).
[24] A. J. Koning and J. P. Delaroche, Nucl. Phys. A **713**, 231 (2003).
[25] G. L. Wales and R. C. Johnson, Nucl. Phys. A **274**, 168 (1976).
[26] L. Trache, A. Azhari, F. Carstoiu, C. A. Gagliardi, A. M. Mukhamedzhanov, X. D. Tang, R. E. Tribble, and S. Zhou, Tex. A&M Cyclotron Prog. Rep. **1**, 16 (2002).
[27] N. K. Timofeyuk, D. Baye, P. Descouvemont, R. Kamouni, and I. J. Thompson, Phys. Rev. Lett. **96**, 162501 (2006).
[28] D. Y. Pang, F. M. Nunes, and A. M. Mukhamedzhanov, Phys. Rev. C **75**, 024601 (2007).
[29] N. C. Summers and F. M. Nunes, Phys. Rev. C **78**, 069908(E) (2008).
[30] A. M. Mukhamedzhanov, V. Burjan, M. Gulino, Z. Hons, V. Kroha, M. McCleskey *et al.*, Phys. Rev. C **84**, 024616 (2011).
[31] V. Maddalena, T. Aumann, D. Bazin, B. A. Brown, J. A. Caggiano *et al.*, Nucl. Phys. A **682**, 332 (2001).
[32] E. Sauvan, F. Carstoiu, N. A. Orr, J. C. Angélique, W. N. Catford *et al.*, Phys. Lett. B **491**, 1 (2000).
[33] N. C. Summers and F. M. Nunes, Phys. Rev. C **78**, 011601(R) (2008).
[34] J. Nolen and J. Schiffer, Annu. Rev. Nucl. Sci. **19**, 471 (1969).
[35] H. T. Fortune, Phys. Rev. C **74**, 054310 (2006).
[36] H. T. Fortune and R. Sherr, Eur. Phys. J. A **47**, 154 (2011).
[37] H. T. Fortune and R. Sherr, Phys. Rev. C **72**, 024319 (2005).
[38] D. J. Millener, Nucl. Phys. A **693**, 394 (2001).
[39] A. Deltuva, Phys. Rev. C **79**, 054603 (2009).
[40] A. M. Mukhamedzhanov, B. F. Irgaziev, V. Z. Goldberg, Y. V. Orlov, and I. Qazi, Phys. Rev. C **81**, 054314 (2010).
[41] V. Z. Goldberg, G. G. Chubarian, G. Tabacaru, L. Trache, R. E. Tribble, A. Aprahamian, G. V. Rogachev, B. B. Skorodumov, and X. D. Tang, Phys. Rev. C **69**, 031302 (2004).

[42] W. A. Peters, T. Baumann, D. Bazin, B. A. Brown, R. R. C. Clement, N. Frank, P. Heckman, B. A. Luther, F. Nunes, J. Seitz, A. Stolz, M. Thoennessen, and E. Tryggestad, Phys. Rev. C **68**, 034607 (2003).
[43] A. M. Mukhamedzhanov, Phys. Rev. C **84**, 044616 (2011).
[44] A. S. Kadyrov, I. Bray, A. M. Mukhamedzhanov, and A. T. Stelbovics, Ann. Phys. **324**, 1516 (2009).
[45] I. Bray, D. V. Fursa, A. S. Kadyrov, A. T. Stelbovics, A. S. Kheifets, and A. M. Mukhamedzhanov, Phys. Rep. **520**, 135 (2012).
[46] C. A. Bertulani, Comput. Phys. Commun. **156**, 123 (2003).
[47] A. Horvath, J. Weiner, A. Galonsky, F. Deak, Y. Higurashi *et al*., Astrophys. J. **570**, 926 (2002).